

A Millimeter-Wave Mutual-Coupling-Resilient Double-Quadrature Transmitter for 5G Applications

Pashaeifar, Masoud; Vreede, Leo C. N. de; Alavi, Morteza S.

DOI

[10.1109/JSSC.2021.3111126](https://doi.org/10.1109/JSSC.2021.3111126)

Publication date

2021

Document Version

Accepted author manuscript

Published in

IEEE Journal of Solid-State Circuits

Citation (APA)

Pashaeifar, M., Vreede, L. C. N. D., & Alavi, M. S. (2021). A Millimeter-Wave Mutual-Coupling-Resilient Double-Quadrature Transmitter for 5G Applications. *IEEE Journal of Solid-State Circuits*, 56(12), 3784-3798. Article 9540036. <https://doi.org/10.1109/JSSC.2021.3111126>

Important note

To cite this publication, please use the final published version (if applicable).
Please check the document version above.

Copyright

Other than for strictly personal use, it is not permitted to download, forward or distribute the text or part of it, without the consent of the author(s) and/or copyright holder(s), unless the work is under an open content license such as Creative Commons.

Takedown policy

Please contact us and provide details if you believe this document breaches copyrights.
We will remove access to the work immediately and investigate your claim.

A Millimeter-Wave Mutual-Coupling-Resilient Double-Quadrature Transmitter for 5G Applications

Masoud Pashaeifar^{ID}, *Student Member, IEEE*, Leo C. N. de Vreede^{ID}, *Senior Member, IEEE*, and Morteza S. Alavi^{ID}, *Member, IEEE*

Abstract—This article presents a wideband energy-efficient transmitter (TX) for 5G mm-wave phased-array systems. It features an advanced double-quadrature direct upconverter (DQ-DUC) to improve its in-band linearity and spectral purity. The proposed TX architecture incorporates an efficiency-enhanced balanced power amplifier (EEBPA) that mitigates VSWR fluctuations in phased-array systems while enhancing efficiency at power back-off (PBO). The EEBPA comprises two identical series-Doherty power amplifiers (PAs) combined through a quadrature hybrid coupler forming a balanced PA. The proposed DQ-DUC consists of a pair of I/Q modulators and the proposed EEBPA's quadrature combiner to further suppress the I/Q image. To verify the proposed techniques, a 40-nm CMOS prototype is implemented. It delivers 20 dBm $P_{1\text{dB}}$ with 40%/31% drain efficiency at $P_{1\text{dB}}$ /6-dB PBO. The measured TX output reflection coefficient is better than -18 dB over a 22.5–30-GHz band. Its intrinsic LO feedthrough and image-rejection ratio for a 100-MHz tone spacing over a 24–30-GHz band are better than -45 dB/50 dB, respectively, without calibration. The average error vector magnitude (EVM) is better than -27.1 dB without digital pre-distortion for an eight-carrier “100-MHz 64-QAM OFDM” signal with an 800-MHz aggregated bandwidth while generating an average output power of 8.4 dBm with 10.8% drain efficiency. Its maximum forward-power/EVM deviations are better than 0.3/1.65 dB, respectively, for a “100-MHz 64-QAM” signal under a voltage standing wave ratio of 3.

Index Terms—Balanced power amplifier (PA), calibration free, direct upconverter, double-quadrature, image-rejection ratio (IRR), mutual-coupling, series-Doherty PA, transmitter (TX).

I. INTRODUCTION

MILLIMETER-WAVE (mm-wave) communication systems have been considered as key enablers for developing the fifth generation (5G) of a mobile network offering high data throughput, low network latency, and improved link robustness [1]–[4]. Taking advantage of mm-wave phased arrays empowers 5G communication systems to establish directional links with large bandwidth between the base station

Manuscript received April 22, 2021; revised July 28, 2021; accepted August 27, 2021. This article was approved by Associate Editor Nagendra Krishnapura. This work was supported by the NWO/NXP 5G Partnership Project 15593. (Corresponding author: Masoud Pashaeifar.)

The authors are with the Department of Microelectronics, Delft University of Technology, 2628 CD Delft, The Netherlands (e-mail: m.pashaeifar@tudelft.nl; l.c.n.devreede@tudelft.nl; s.m.alavi@tudelft.nl).

Color versions of one or more figures in this article are available at <https://doi.org/10.1109/JSSC.2021.3111126>.

Digital Object Identifier 10.1109/JSSC.2021.3111126

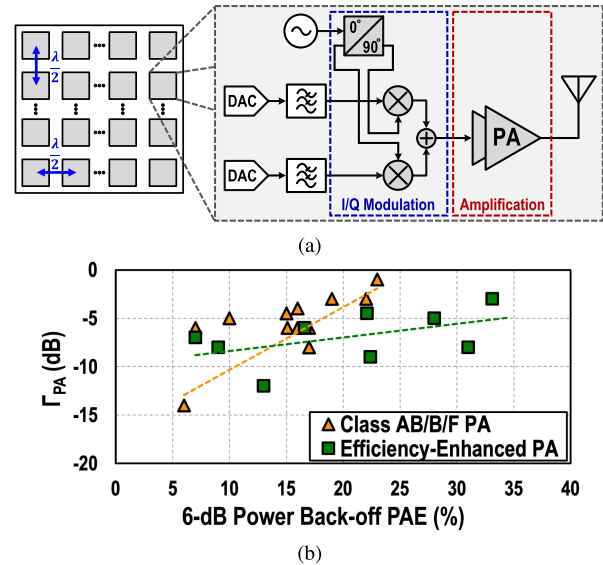


Fig. 1. (a) Conventional Cartesian TX architecture employed in a digital-beamforming phased-array system. (b) Recently published PA's output matching versus their 6-dB PBO PAEs.

and user equipment. To realize such a high data-rate communication link, 5G transmitters (TXs) typically employ spectrally efficient complex modulation schemes with high peak-to-average power ratios (PAPRs) [5]. However, this feature entails operation at a power back-off (PBO), imposing stringent requirements on the TX modulation accuracy, spectral purity, and PBO efficiency.

Fig. 1(a) shows a conventional Cartesian TX architecture employed in a digital-beamforming phased-array system [6]. It comprises two distinct parts: 1) a wideband in-phase/quadrature (I/Q) modulator, which needs to provide low error vector magnitude (EVM) to facilitate multi-Gb/s high-order complex modulations and 2) a highly energy-efficient RF power amplifier (PA) to properly boost its radiated power, addressing the required link budget.

In this architecture, the I/Q modulators must exhibit minimal I/Q imbalance and LO feedthrough (LOFT) to yield low-EVM modulation [7]. These requirements are challenging when operating at the mm-wave bands due to employing relatively small transistors and passive components that are extremely sensitive to process, voltage, and temperature (PVT)

variations [8]. A typical solution is adopting I/Q and LOFT calibrations that require complicated and exhaustive search methods [9]–[15]. Consequently, an I/Q TX architecture with inherently low I/Q imbalance and LOFT is highly desirable, especially in the context of the large-scale 5G mm-wave phased-array systems [16].

On the other hand, the 5G link budget demands 60-dBm radiated TX power to cover a relatively short distance [5]. To generate such radiated power, considering 16×16 phased-array antennas, each single antenna element must radiate 12-dBm average power. Consequently, assuming a single patch antenna with 5-dBi antenna gain and 2-dB connection loss, the average/peak TX power should exceed 9/20 dBm for a modulated signal with an 11-dB PAPR. Generating these power levels is challenging, especially in nanoscale bulk CMOS technology with limited supply voltage and operating frequency. Stacked-FET PAs and power combining TX architectures are widely used to generate more than 20-dBm peak power [17]–[24]. In addition, efficiency enhancement techniques, such as Doherty PAs and out-phasing TXs, can simultaneously offer high output power and high average efficiency for modulation schemes with high PAPRs [25]–[38].

Nevertheless, as depicted in Fig. 1(b), employing efficiency-enhanced techniques exacerbates the PA's output reflection coefficient (Γ_{PA}), making them inevitably sensitive to the voltage standing wave ratio (VSWR) of the antenna and its connection. Unfortunately, this becomes even worse in practical situations in which the mutual coupling among the closely spaced antennas yields a beam-steering angle-dependent and time-varying VSWR condition [39]–[43]. In other words, the unwanted element-to-element coupled signal reflects to the antenna, radiates alongside the desired signal, and, subsequently, deteriorates the phased-array beam pattern and TX linearity. A previously promoted solution for this antenna VSWR problem is load mismatch detection followed by tuning of the output matching network (self-healing) [44]. However, this technique requires the use of a reconfigurable and inevitable lossy matching network. Furthermore, active load pulling [45] and using a reconfigurable series/parallel Doherty PA structure [34] are proposed to realize a VSWR resilient efficiency-enhanced TX. Nevertheless, all these techniques are only suitable when dealing with a known and stable antenna impedance mismatch, which is, unfortunately, not the case in practical situations.

A conventional solution for a VSWR resilient PA is employing an isolator at its output. Due to the area constraint of the phased-array transceivers, an integrated isolator would be a viable solution. However, the integrated state-of-the-art mm-waves circulators/isolators [46]–[48] occupy a large area ($>1.3 \text{ mm}^2$) compared to the designated area of the whole transceiver [16]. Moreover, they demonstrate high TX-to-antenna loss ($>3.2 \text{ dB}$) and require extra power consumption to generate their quadrature clocks. Recently, balanced PAs (BPAs) are used at mm-wave to mitigate VSWR condition but still suffer from low PBO drain efficiency [49], [50].

In [51], we recently proposed a TX architecture with an efficiency-enhanced BPA (EEBPA) combiner. It consists of

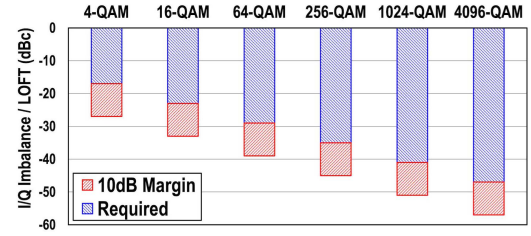


Fig. 2. Required LOFT and I/Q imbalance for various modulation schemes considering 10-dB margin.

two identical series-Doherty PAs combined through a quadrature hybrid coupler (QHC) forming a BPA. The quadrature combiner has three crucial roles in this architecture: 1) combine the output of two Doherty PAs to achieve the desired output power; 2) suppress output injected wave, resulting from mutual-coupling, by offering close to perfect matching conditions; and 3) act as a second image-rejection stage and provide a calibration-free low I/Q imbalance modulation.

This article investigates architectural analysis and elaborates on the system- and circuit-level design considerations and extensive measurement results. It is organized as follows. Section II presents the proposed double-quadrature direct-upconversion TX architecture and investigates its performance under process variation. The EEBPA is presented in Section III. Circuit implementation details of the proposed TX are described in Section IV. Section V presents the measurement results, and Section VI concludes this article.

II. DOUBLE-QUADRATURE I/Q MODULATOR

The 5G communication systems employ spectrally efficient modulation schemes, such as 64- and 256-QAM signals. Exploiting these complex modulated signals entails meeting stringent TX in-band linearity requirements verified by EVM, which comprises quantization noise, phase noise, I/Q modulation imbalance, LOFT, and the PA non-linearity¹ [5], [8]. Fig. 2 shows the required LOFT and I/Q imbalance for various modulation schemes assuming an ideal condition for the remaining EVM contributors. The required I/Q imbalance/LOFT for 64-QAM and 256-QAM are -29 and -35 dBc, respectively. Therefore, the design specs are defined considering a 10-dB margin to include the non-ideality effect of the remaining EVM contributors. However, achieving a better than 10-dB margin will relax the required specs of the other parts of the system, such as PA and PLL, resulting in better system efficiency. Consequently, the first design challenge is obtaining calibration-free I/Q imbalance/LOFT < -45 dBc and eventually diminishing the I/Q imbalanced performance even further.

A conventional approach for generating highly accurate quadrature LO signals that seamlessly operate in the

¹The overall EVM of the TX can be estimated by

$$\text{EVM}_{\text{TX}} = \sqrt{\text{EVM}_{\text{DAC}}^2 + \text{EVM}_{\text{P.N.}}^2 + \text{EVM}_{\text{IRR}}^2 + \text{EVM}_{\text{LOFT}}^2 + \text{EVM}_{\text{PA}}^2}$$

where EVM_{DAC} , $\text{EVM}_{\text{P.N.}}$, EVM_{IRR} , EVM_{LOFT} , and EVM_{PA} are the EVM degraded by quantization noise, phase noise, I/Q modulation imbalance, LOFT, and the PA non-linearity, respectively.

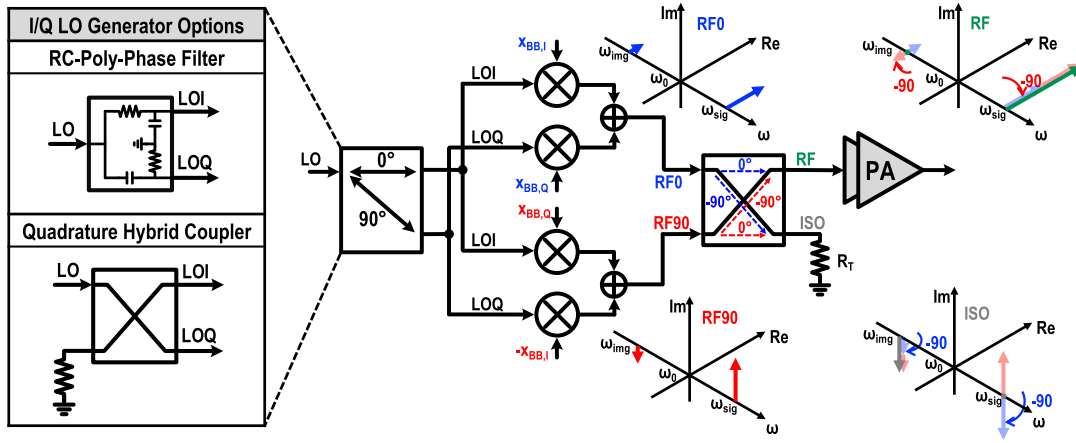


Fig. 3. DQ-DUC concept. The LO generator could be either an *RC* PPF or a QHC.

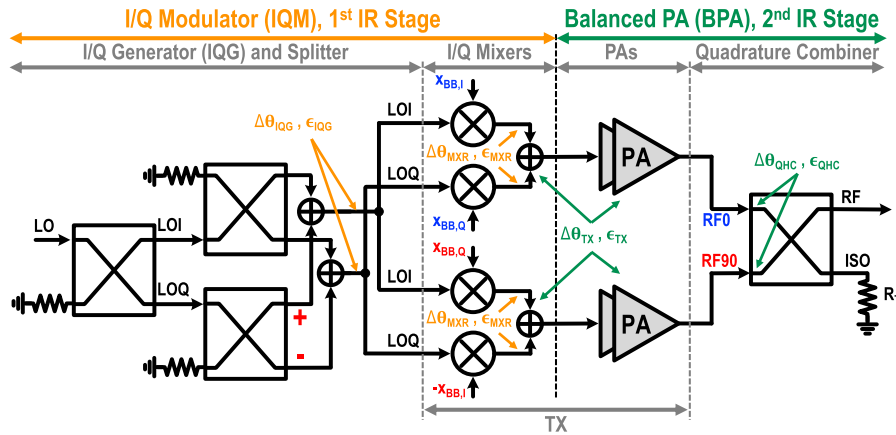


Fig. 4. Proposed DQ-DUC with two-stage I/Q LO generator. The contribution of each part in IRR has been shown.

24–30-GHz 5G mm-waveband comprises a multistage *RC* poly-phase filter (PPF) [52]. Although this approach has a small footprint, it is susceptible to inductive/capacitive parasitics and temperature variations [8]. Recently, multistage transformer-based QHCs are widely used at mm-wave bands with reasonable die-area [53], [54]. However, even though the quadrature accuracy of the LO signals was close to a perfect condition, the interconnect parasitics and device mismatch significantly degrade the I/Q modulator's performance at the designated mm-waveband. Thus, employing I/Q calibration is inevitable, which increases the system complexity. In addition, large-scale digital/hybrid beamforming phased-array systems demand high yield and minimal system complexity [16].

Double-quadrature receiver architectures are a well-known structure to mitigate IRR [55], commonly used in two-step down-conversion topologies [56], [57]. In this section, we first present the direct double-quadrature upconversion concept. Afterward, by employing Monte Carlo (MC) simulations, the yield of the proposed architecture will be investigated.

A. Double-Quadrature Direct-Upconversion Concept

Fig. 3 conceptually illustrates a double-quadrature direct upconverter (DQ-DUC). The DQ-DUC comprises an I/Q modulator, acting as the first image-reject filter, and a quadrature

combiner, operating as the second image-reject filter. The I/Q modulator consists of an I/Q LO generator, either a PPF or a QHC, followed by a pair of I/Q mixers whose baseband inputs of the bottom I/Q mixer are swapped, while its in-phase signal, $x_{BB,I}$, is negated. As a result, the desired signals' phase excursion at the output of these mixers is $+90^\circ$ out of phase, while their image signals have a phase difference of -90° (see Fig. 3).

Subsequently, by employing an isolated quadrature combiner, e.g., a QHC, with a constant -90° phase shift, the desired signals are constructively combined at the output port, whereas the image signals are canceled (see Fig. 3). The opposite operation occurs at the isolation port. The mathematical relationship is derived in Appendix A.

B. Double-Quadrature Direct-Upconversion TX Architecture

The proposed TX architecture is depicted in Fig. 4. A two-stage transformer-based QHC is employed as an I/Q generator (IQG) to minimize I/Q imbalance and widen operational frequency [54]. The output QHC and its following PA (see Fig. 4) are swapped to establish a BPA. The motivation for this PA structure will be further explained in Section III. The image-rejection ratio (IRR) of the I/Q modulator (IRR_{IQM}), which is the first image rejection stage, is determined by the

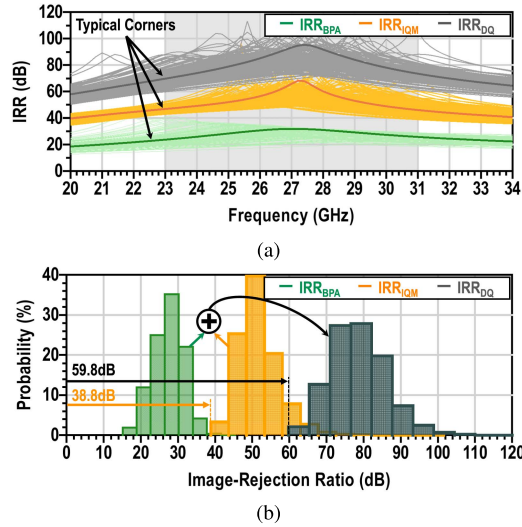


Fig. 5. (a) IRR of I/Q modulator, BPA, and overall TX over 200 trials of an MC simulation. (b) IRR resulted from an MC at 23–31-GHz band. The overall IRR is always higher than 59.8 dB.

amplitude and phase inaccuracy of IQG ($\epsilon_{IQG}, \Delta\theta_{IQG}$) and I/Q mixers ($\epsilon_{MXR}, \Delta\theta_{MXR}$)

$$IRR_{IQM} = f(\epsilon_{IQG}, \epsilon_{MXR}, \Delta\theta_{IQG}, \Delta\theta_{MXR}). \quad (1)$$

It is worth mentioning that the device and interconnection mismatch of mm-wave I/Q mixers play an equally important role as that of the LO I/Q imbalance [8]. Nevertheless, increasing the IQG's number of cascaded stages does not necessarily improve the IRR_{IQM} , which is already constrained by mixers' mismatches. Fig. 5(a) shows the IRR_{IQM} based on 200 MC simulations where the active parts are modeled as ideal components with their relative mismatches to speed up simulation time. In addition, the mismatch of all passive components, such as capacitors and resistors, is considered in these simulations.

The IRR of the BPA (IRR_{BPA}), the second IR stage, can be calculated by mismatches of top and bottom TX paths ($\epsilon_{TX}, \Delta\theta_{TX}$), and I/Q imbalance of QHC ($\epsilon_{BPA}, \Delta\theta_{BPA}$)

$$IRR_{IQM} = f(\epsilon_{TX}, \epsilon_{BPA}, \Delta\theta_{TX}, \Delta\theta_{BPA}). \quad (2)$$

The MC simulation results for IRR_{BPA} and overall IRR (IRR_{DQ}) are shown in Fig. 5 and can be expressed as

$$IRR_{DQ} = IRR_{IQM} \times IRR_{BPA}. \quad (3)$$

According to (1) and (2), the IRR_{IQM} and IRR_{BPA} are uncorrelated. Consequently, although they might not meet the aimed mismatch performance individually, their combined performances satisfy the overall designated IRR. Therefore, the proposed approach relaxes the mismatch requirement and makes this architecture less sensitive to PVT variations than a conventional structure for the same overall targeted IRR.

III. EFFICIENCY-ENHANCED BALANCED PA

In a phased-array TX front-end, two impedance mismatch mechanisms affect the PA/TX performance: 1) antenna

impedance mismatch and 2) mutual coupling. Fig. 6(a) illustrates forward and reverse waves of the PA and its antenna. In this context, the antenna impedance mismatch, including its transmission line connector, is modeled as a two-port passive component, which indicates that the antenna is considered a perfectly matched port. As depicted in Fig. 6(b), alongside the PA represented as a Norton equivalent source, we have also modeled the mutual-coupling signal as a secondary power source at the antenna port. Since the mutual-coupling signal is correlated with the PA signal and the antenna is considered as an ideal port, the antenna's forward voltages can be expressed as

$$a_2 = S_{MC}a_1 \quad (4)$$

where a_1 is PA's forward signal when $a_2 = 0$ and S_{MC} is a time-varying element-to-element coupling coefficient, depending on the beam-steering angle.

The reverse waves and impedances seen by the PA are shown in Fig. 6(c) for three different cases: 1) only antenna impedance mismatch; 2) only mutual-coupling signal; and 3) antenna impedance mismatch and mutual-coupling signal. In a large-scale phased-array TX with narrow beamwidth capability, the radiated signal robustness of each antenna element is essential for beamforming accuracy. This indicates that the radiated signal, i.e., b_2 , must stay relatively stable during beamforming, as shown in Fig. 6. However, in the presence of the mutual coupling alongside the desired signal, $S_{MC} a_1$, the time-varying reflected mutual-coupling signal, i.e., $(S_{22} + S_{12}S_{21}\Gamma_{PA})S_{MCA1}$, is radiated, deteriorating the beam pattern. Therefore, S_{22} and Γ_{PA} must be relatively small.

On the other hand, although the efficiency and overall TX performance benefit from small S_{11}/S_{22} , small Γ_{PA} leads to low PBO efficiency [see Fig. 1(b)]. Thus, our motivation is to design a PA structure with high PBO efficiency and relatively low Γ_{PA} . Moreover, as illustrated in the last column of Fig. 6(c), when a PA experiences a large VSWR condition, its stability, efficiency, and output power deteriorate significantly. This section presents the proposed VSWR resilient EEBPA for mm-wave phased-array systems.

A. Proposed Efficiency-Enhanced Balanced PA

As depicted in Fig. 7, the proposed EEBPA consists of two identical efficiency-enhanced PAs (EEPAs) combined through a QHC. The PAs can be Doherty, out-phasing, or any other efficiency-enhanced structure. In the proposed PA architecture, the EEPAs perform PBO efficiency enhancement, whereas the BPA combiner provides VSWR resilience. To validate the proposed PA's output matching, as mentioned before, we modeled the mutual-coupling signal as a power source at the antenna port. As illustrated in Fig. 8(a), the unwanted coupled signal, i.e., "a_{MC}," is split by the hybrid coupler reflected from PAs, constructively added at the isolation port, and eventually absorbed in the 50-Ω termination. However, the reflected waves are canceled at the antenna port. Consequently, " Γ_{BPA} " is zero if the EEPAs are identical ($\Gamma_{PA1} = \Gamma_{PA2}$), and the hybrid coupler is an ideally symmetric structure.

Assuming two identical PAs, Fig. 8(b) depicts the forward and reflected waves of each PA in the steady state.

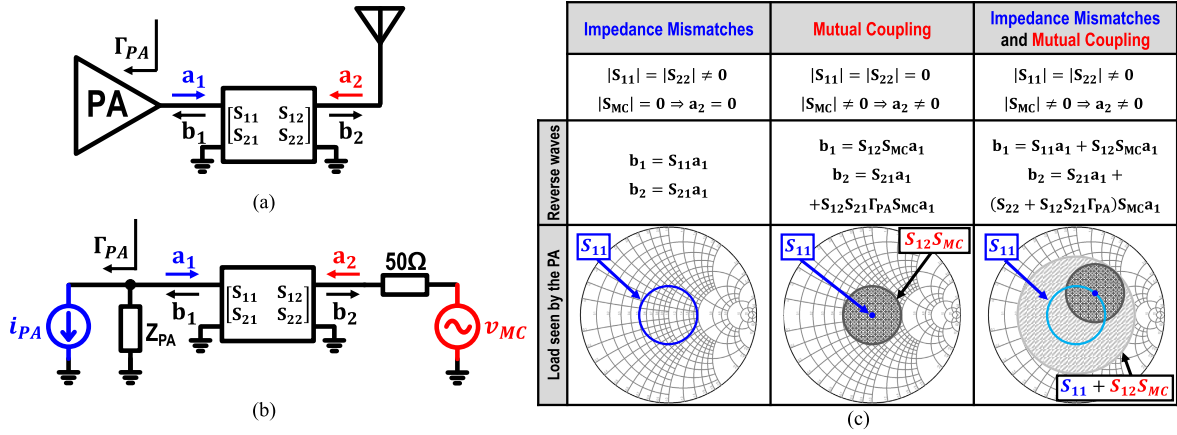


Fig. 6. (a) Forward and reverse waves of the PA and antenna, where the connection and antenna mismatches are modeled as a two-port passive component. (b) Norton model represents PA, whereas the mutual-coupling signal is modeled as a secondary power source at the antenna. (c) Reverse waves and impedances seen by PA for three cases: 1) only antenna impedance mismatches; 2) only mutual-coupling signal; and 3) antenna impedance mismatches and mutual-coupling signal.

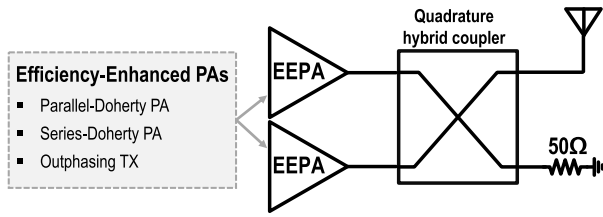


Fig. 7. Proposed EEBPA structure.

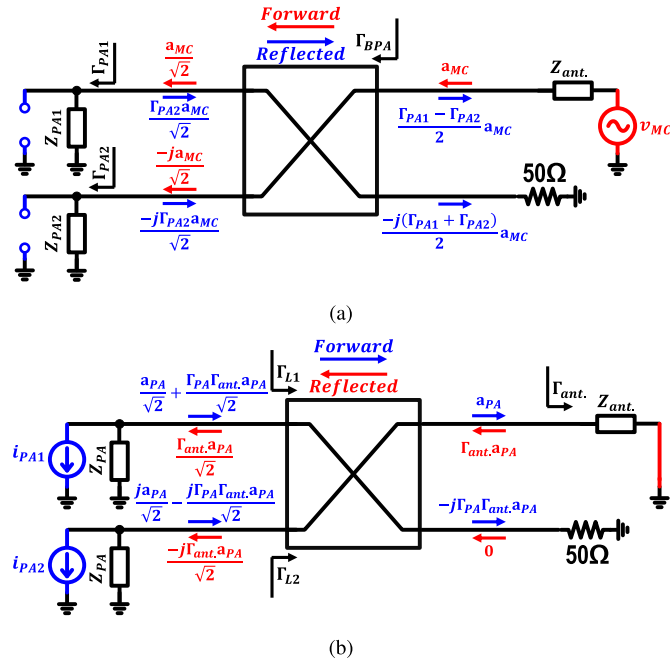


Fig. 8. Forward and reflected waves in (a) mutual-coupling and (b) TX scenarios.

The PAs' forward wave consists of two parts. The first part is the desired signals with 90° out of phase ($(a_{PA}/\sqrt{2})$ and $(ja_{PA}/\sqrt{2})$) that are eventually combined at the output

port (a_{PA}). However, due to antenna impedance mismatch, part of the desired signal reflects ($\Gamma_{ant}a_{PA}$). The hybrid coupler splits this reflected signal into two waves ($\Gamma_{ant}a_{PA}/\sqrt{2}$ and $(-j\Gamma_{ant}a_{PA}/\sqrt{2})$), and then, they proceed to the PAs' ports. Note that Γ_{PA} and Γ_{ant} are the reflection coefficient of the PAs and the antenna, respectively.

On the other hand, the second part of PAs' forward signals are proportional to the antenna mismatch that are reflected from the PAs ($(\Gamma_{PA}\Gamma_{ant}a_{PA}/\sqrt{2})$ and $(-j\Gamma_{PA}\Gamma_{ant}a_{PA}/\sqrt{2})$). Since the signals are -90° out of phase, they are combined and absorbed at the termination port as in the case of the mutual coupling scenario. Hence, the load seen by each PA can be calculated as

$$\Gamma_{L1} = \frac{\Gamma_{ant} \frac{a_{PA}}{\sqrt{2}}}{\frac{a_{PA}}{\sqrt{2}} + \Gamma_{PA} \Gamma_{ant} \frac{a_{PA}}{\sqrt{2}}} = \frac{\Gamma_{ant}}{1 + \Gamma_{PA} \Gamma_{ant}} \quad (5)$$

$$\Gamma_{L2} = \frac{\Gamma_{ant} \frac{-ja_{PA}}{\sqrt{2}}}{\frac{ja_{PA}}{\sqrt{2}} + \Gamma_{PA} \Gamma_{ant} \frac{-ja_{PA}}{\sqrt{2}}} = \frac{-\Gamma_{ant}}{1 - \Gamma_{PA} \Gamma_{ant}} \quad (6)$$

As a result, the forward wave of the balanced amplifier is always constant [i.e., a_{PA} , depicted in Fig. 8(b)], independent of antenna's and PAs' impedances. Besides, the delivered power to the antenna is determined by the antenna mismatch loss ($1 - |\Gamma_{ant}|^2$). This, in turn, degrades drain efficiency. Nevertheless, the unmatched loading condition can degrade the delivered power and efficiency further in the large-signal operation, where a large impedance leads to an early power saturation condition for the PAs. For further elaboration, we assume two extreme cases: 1) the PAs are impedance matched to characterization impedance of hybrid coupler ($Z_{PA} = Z_0 \Rightarrow \Gamma_{PA} = 0$) and 2) the PAs are ideal current sources ($Z_{PA} = \infty \Rightarrow \Gamma_{PA} = 1$).

- 1) $\Gamma_{PA} = 0$: In this case, $\Gamma_{L1} = \Gamma_{ant}$ and $\Gamma_{L2} = -\Gamma_{ant}$. It means one of the PAs drives Z_{ant} , while the other one drives (Z_0^2/Z_{ant}) . This balanced loading condition makes the proposed EEBPA relatively robust against VSWR in large-signal operations where only one of the PAs can be saturated by the large load impedance.

- 2) $\Gamma_{PA} = 1$: In this case, which is a more practical assumption, $\Gamma_{L1} = (\Gamma_{ant.}/1 + \Gamma_{ant.})$ and $\Gamma_{L2} = (-\Gamma_{ant.}/1 - \Gamma_{ant.})$. Even though the reflection coefficients are not equal in magnitude, they are still in opposite signs. Hence, the magnitude of the impedance seen by one of the PAs is always equal to or larger than $\sqrt{1 + |2\Gamma_{ant.}|^2} Z_0$. Likewise, the other load impedance is equal to or smaller than $\sqrt{1 + |2\Gamma_{ant.}|^2} Z_0$.

In summary, operating in PBO, the proposed EEBPA offers a close to perfect termination for an impedance mismatch caused by a mutual-coupling signal. Moreover, it limits the delivered power degradation to mismatch losses presented by static antenna mismatch. Furthermore, the analysis shows that, even in the near power saturation operation, by providing a balanced loading condition, the proposed structure diminishes forward power deviation, delivered power loss, and efficiency degradation in both mutual-coupling and impedance mismatch scenarios [58]. The Z-parameter analysis of the balanced amplifier is presented in Appendix B.

In terms of stability, according to (5) and (6), if $|\Gamma_{ant.}| > |1 \pm \Gamma_{PA}\Gamma_{ant.}|$, one of the PAs' load impedances is negative, which may lead to an unstable state. In the extreme case of $\Gamma_{PA} = 1$, this undesired condition is occurred if $|\text{Re}(\Gamma_{ant.})| > 0.5$. Nevertheless, in practice, $|\Gamma_{PA}| < 1$ and the loss of QHC reduce the risk of a negative load impedance.

B. Series-Doherty Balanced PA

To realize the efficiency-enhanced PA, we chose a Doherty PA. The most common structure is a parallel-Doherty PA, which has frequency-dependent output power [59], making it less suitable for broadband operation. Consequently, in this work, a series-Doherty PA structure is selected. Compared to the parallel configuration, the series-Doherty PA ideally provides a frequency-independent output power, as well as, lower impedances to its PAs, features that are highly desirable to obtain sufficient output power from a CMOS technology with a low breakdown voltage [38].

IV. CIRCUIT IMPLEMENTATION

The proposed double-quadrature direct-upconversion TX is implemented in 40-nm bulk CMOS technology. The chip occupies an area of 2.08 mm \times 1.76 mm, while its core area is 0.96 mm \times 1.44 mm (see Fig. 9). Fig. 10 exhibits a detailed schematic of the overall TX architecture. It consists of four sub-TXs; each comprises a double-balanced I/Q active mixer, a pre-driver (DRV), and a PA. Each pair of sub-TXs is connected to a series-Doherty power combiner. Subsequently, their outputs are combined with a 50- Ω QHC to realize the overall BPA while simultaneously acting as a second image rejection stage of the DQ-DUC. Moreover, a two-stage transformer-based QHC is adopted [54] to increase the TX operational frequency. Since the IQG should provide I/Q LO signals for four sub-TXs, to avoid a one-to-four power splitter, two identical two-stage QHCs have been implemented. Note that the IQG's ports are directly connected to the I/Q mixers without employing any termination to increase voltage gain and diminish the circuit complexity [54]. Moreover, an LO

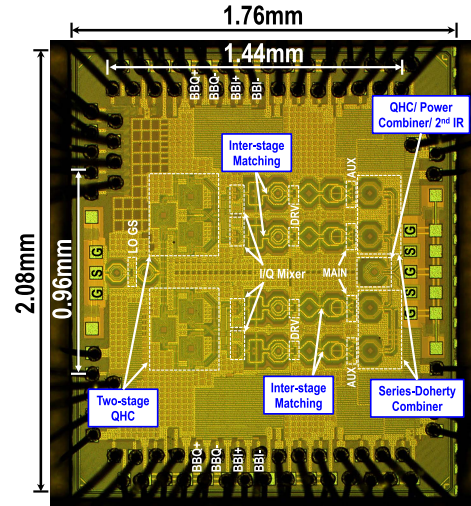


Fig. 9. Die micrograph of the proposed TX.

gain stage (GS) is employed to bring the external LO signal's level (0 dBm) to the required level.

The measured power consumption of each part is summarized in Fig. 10 when the TX average output power is 14 dBm at 27 GHz. The PAs and their pre-drivers consume 133 mW, i.e., 69% of the total power while delivering 25 mW to the load. Moreover, the active mixers and LO GS dissipate 30.9 and 28.5 mW, respectively; namely, the power consumption of each mixer is 7.7 mW.

Fig. 11 shows the schematic and S-parameter simulation results of the output QHC. Its insertion loss is 0.55 dB while providing more than 22-dB isolation between two PAs. Furthermore, the series-Doherty PAs are connected to QHC by two 50- Ω coplanar transmission lines that add an extra 0.25-dB loss. Fig. 12 illustrates the layout and schematic of the series-Doherty combiner. A two-step transformer-based impedance inverter is implemented in the auxiliary path of the proposed series-Doherty combiner to perform load modulation. The combiner consists of two identical transformers connected by a lumped-element transmission line providing a 50° phase shift. The capacitors at the primary side of transformers are absorbed in the parasitic capacitors of the PAs. Therefore, only a 220-fF capacitor is placed at the secondary side of the auxiliary transformer. Compared to a conventional single CLC π -network, a two-step transmission line offers lower loss and broader bandwidth. It is worth mentioning that the metal slotting technique [60] is employed to increase the quality factor (Q) of the transformer due to reducing the skin effect [see Fig. 12(a)]. In addition, the secondary (sec.) is placed between the two slots of the primary (prim.) to boost the coupling factor.

In each Doherty branch, the PA, pre-driver, I/Q mixer, inter-stage matching networks, and most of their biases are the same for main and auxiliary paths. However, in the auxiliary path, the pre-driver and PA biases are modulated by the adaptive biasing circuit to perform the Doherty operation. Fig. 13 depicts the detailed schematic of PA, pre-driver, and adaptive biasing circuitry [30]. A push-pull common-source

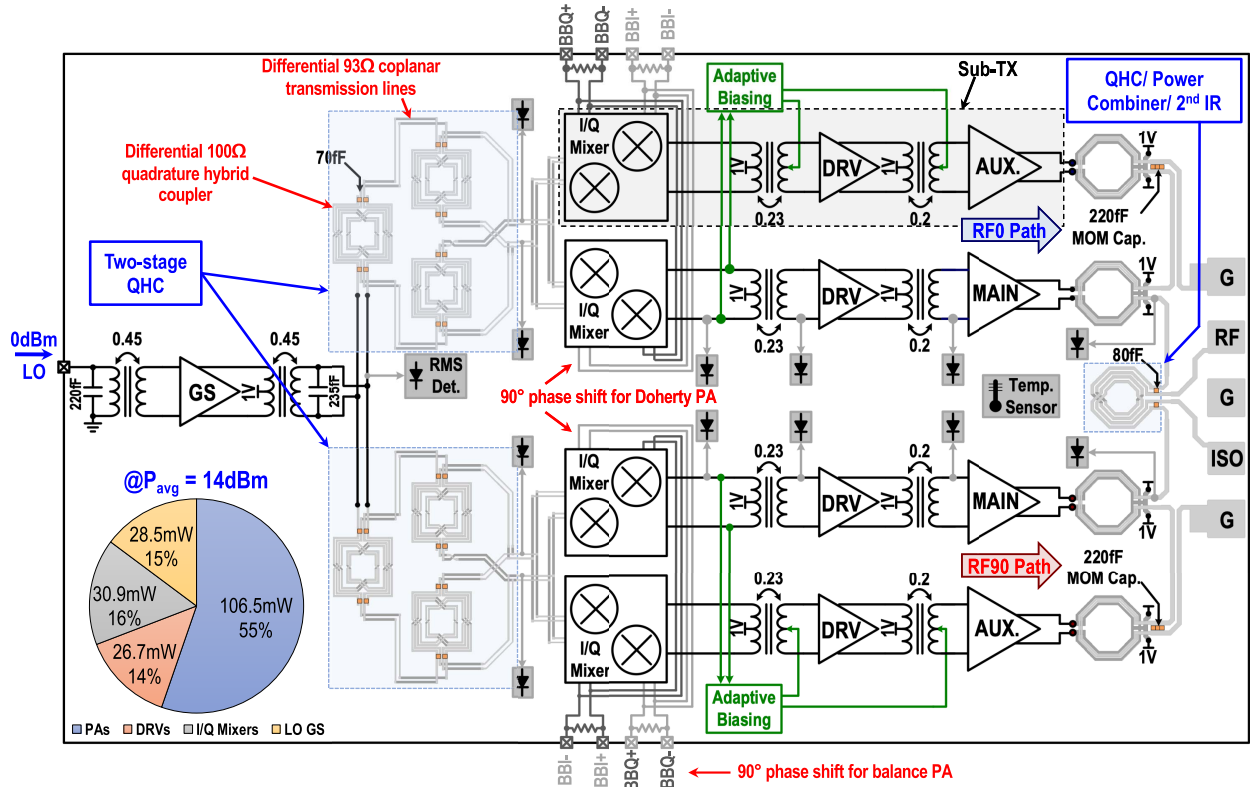


Fig. 10. Detail schematic of overall TX architecture.

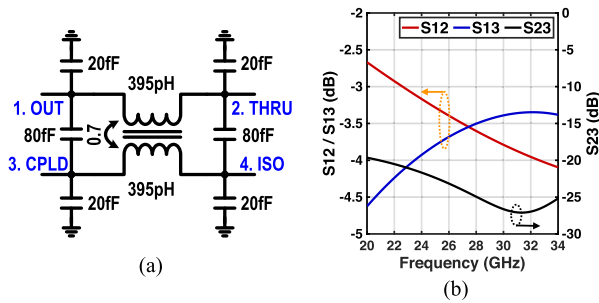


Fig. 11. (a) Schematic of the output QHC and (b) its S-parameter simulation results.

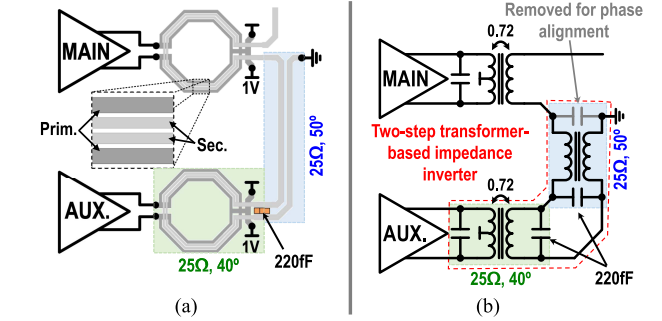


Fig. 12. (a) Layout and (b) schematic of the proposed series-Doherty combiner with the two-step transformer-based impedance inverter.

amplifier with a cross-coupled drain-gate feedback capacitor is exploited to improve stability and reverse isolation. Each transistor consists of eight unit-cells with a transistor aspect ratio of $50 \mu\text{m}/40 \text{ nm}$, which are optimized to mitigate the impact of device parasitics and interconnections [61]. The pre-driver employed the same structure comprising four unit-cells (overall $W/L = 200 \mu\text{m}/40 \text{ nm}$). Besides, two varactors are utilized at the pre-driver and PA inputs to improve their AM-PM profiles and tune the inter-stage matching network [62]. Double-tuned transformers are implemented as the inter-stage matching network. Moreover, the PA/pre-driver transistors contain parasitic capacitors with a relatively high quality factor (Q), indicating that the real part of the input impedance of the PA/pre-driver is large. Therefore, a parallel

resistor is employed at the input of the PA/pre-driver to increase the operational bandwidth and reduce passive loss by lowering the Q of the resonator.

A double-balanced I/Q active mixer is exploited to realize an I/Q modulator with high conversion gain and decent LO leakage performance. Fig. 14 shows the schematic and simplified layout of the I/Q mixer. The baseband transistors are chosen large enough to minimize LOFT. As mentioned before, at mm-wave frequencies to achieve minimum I/Q imbalance and LOFT, the layout symmetry plays a crucial role. As depicted in Fig. 14(b), the I and Q paths are laid out symmetrically. The baseband signals are shielded to minimize mixers' undesired inter-modulation spurs.

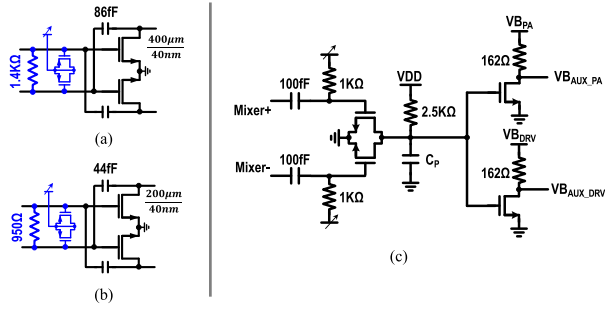


Fig. 13. Schematic of (a) PA, (b) pre-driver, and (c) adaptive-biasing circuit.

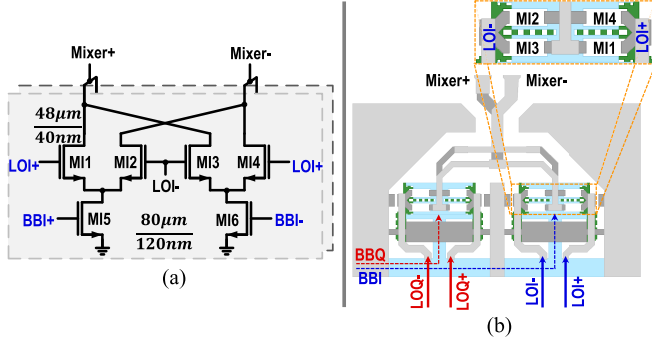


Fig. 14. (a) Schematic and (b) simplified layout of the implemented double-balanced I/Q active mixer.

Embedded voltage root mean square (rms) detectors are utilized to monitor all signal levels of the proposed TX chain from the outputs of the LO GS to the PAs' outputs, represented by the diodes in Fig. 10. Wideband rms detectors, comprising gate-drain connected NMOS transistors biased in the sub-threshold region, are adopted [63]. A temperature sensor, i.e., a diode-connected bipolar transistor, is employed to measure the chip temperature and calibrate the rms detectors.

V. MEASUREMENT RESULTS

All measurements are performed using a high-frequency probe station. The low-frequency pads, including the I/Q baseband signals and dc bias voltages, are wire-bonded directly to an FR4 printed circuit board (PCB). The high-frequency ports comprising the input LO signal and the PA output ports, including the RF and isolation pads, are characterized by GSG and GSGSG probes, respectively. In this work, a 1-V supply voltage is used for the PAs, pre-drivers, mixers, and the LO GS. Fig. 15 exhibits the measurement setup and its baseband connections. A Maury MT984AL load tuner is used for the VSWR measurement. The insertion losses of the probes, cables, and the directional coupler are measured and de-embedded.

A. Continuous-Wave Measurement Results

The input LO and the PA output reflection coefficients are characterized under small-signal conditions using Keysight N5227A four-port network analyzer. Fig. 16 demonstrates the measured s-parameters over a 22–34 GHz band. The

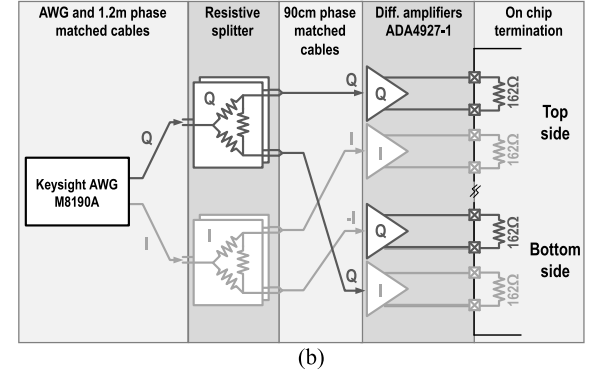
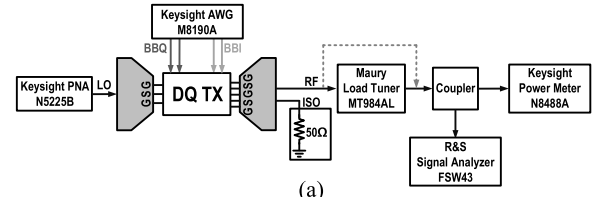


Fig. 15. (a) CW, SSB, modulated signal, and VSWR measurements setup. (b) Baseband connections for the top and bottom sides of TX.

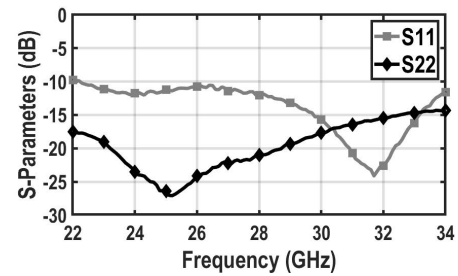


Fig. 16. Small-signal S-parameter measurement results.

corresponding LO port matching is better than -10 dB. The PA's output reflection coefficient, S_{22} , is better than -18 dB over the 22.5–30-GHz band, while, at 27 GHz, it is -22.2 dB. Thus, any unwanted coupled signal at 27 GHz is suppressed by -22.2 dB. Note that, for the isolation port, a 50-Ω termination is employed.

The large-signal continuous-wave (CW) measurement results are reported in Fig. 17. At 26/28 GHz, $P_{1\text{ dB}}$ is 20.1/19.75 dBm, while TX front-end drain efficiency is 28.76/26.4%. Moreover, at 6-dB PBO, the PA drain efficiency is 30/33% at 26 GHz/28 GHz, while the TX conversion gain is 21.8 dB/20.6 dB. As depicted in Fig. 17(c), the TX delivers 20 dBm over a 24–30 GHz (i.e., -1 -dB bandwidth). Over this frequency band, the PA and TX peak drain efficiencies are more than 32.6% and 22.1%, respectively.

B. Single-Sideband Measurement Results

Single-sideband (SSB) measurements evaluate the IRR performance of the proposed TX architecture. Since the double-quadrature structure offers high uncalibrated IRR, I/Q baseband signal mismatches significantly degrade the TX IRR performance. Fig. 15(b) shows the I/Q baseband connections in the measurement setup. These signals are first generated in

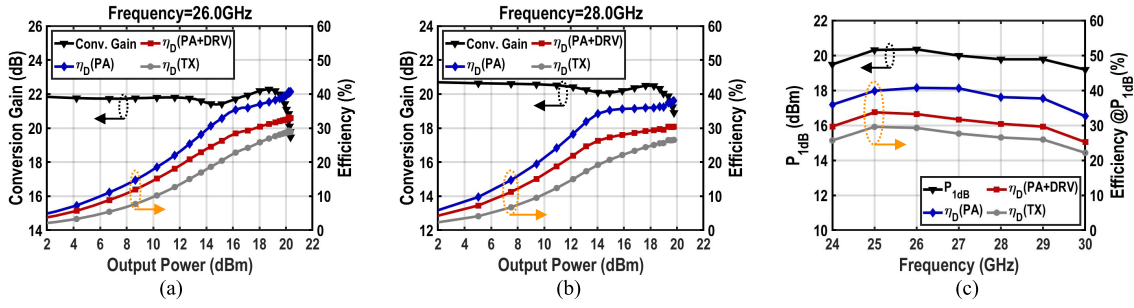


Fig. 17. Large-signal CW measurement results (a) at 26 GHz, (b) at 28 GHz, and (c) across operational frequency.

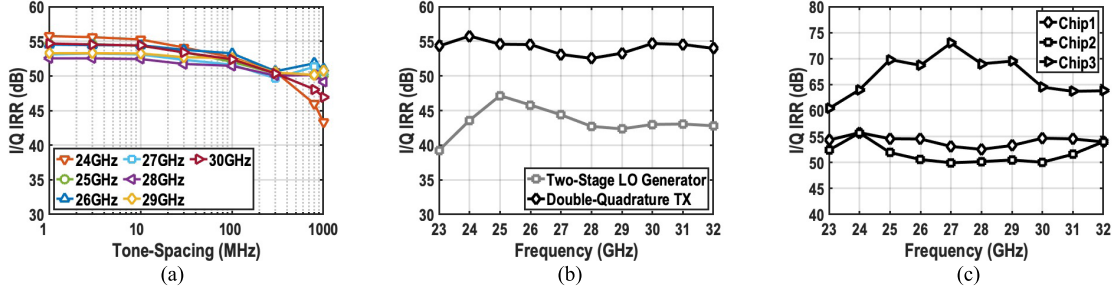


Fig. 18. (a) Measured IRR versus tone spacing across operational frequencies. (b) Measured IRR of two-stage LO generator showing IRR improvement by second IR stage. (c) Measured IIR of three chips versus frequency without any calibration.

MATLAB and then converted to the differential analog signals using an arbitrary-wave generator (AWG).

Fig. 18(a) demonstrates the measured IRR performance versus various tone spacings at 24–30-GHz operational band. The TX achieves an uncalibrated IRR of better than 50 dB over the desired frequency band due to the proposed DQ-DUC technique. Due to the minimal variation of IRR over the frequency band, it can be inferred that the I/Q baseband mismatches, i.e., cables, splitters, amplifiers, on-chip terminations, and baseband transistors of the mixers [see Fig. 15(b)], are the dominant imbalanced sources. Furthermore, by connecting the same I/Q signals to both the top and bottom TX paths, we can disable the second image rejection stage and measure only the IRR performance of the two-stage LO generator. As shown in Fig. 18(b), the second image rejection stage improves IRR by 11 dB on average. However, according to the MC simulations, the IRR improvement should be at least 20 dB, primarily degraded by the I/Q baseband mismatches that are discussed earlier. In addition, as depicted in Fig. 18(c), three chips are validated, proving that the proposed architecture offers more than 50-dB IRR over frequency without any calibration.

The LOFT must be relatively low to achieve decent EVM. Due to the symmetric mixer layout and proper baseband transistors sizing based on the mismatch consideration, the TX attains better than -45 -dB uncalibrated LOFT. The measured LOFTs of three chips are demonstrated in Fig. 19. LOFT variation over frequency shows that the mismatch of high-frequency parts significantly affects the LOFT performance.

C. Modulated Signal Measurement Results

The TX dynamic performance is verified by wideband modulated signals, such as a multi-carrier “64-QAM OFDM”

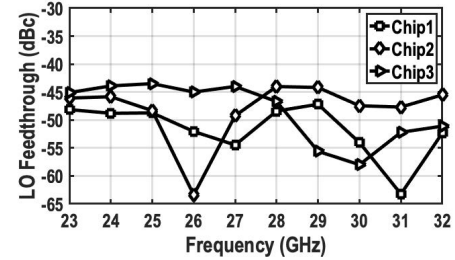


Fig. 19. Measured LOFT of three chips versus frequency without any calibration.

signal. As illustrated in Fig. 15(a), the mm-wave TX output is directly captured by the R&S FSW43 signal analyzer. Fig. 20 exhibits measured constellations, EVMs, and performance of 0.6- and 4.8-Gb/s 64-QAM at 27-GHz carrier frequency. The TX achieves -25.5 -dB EVM for a 0.6-Gb/s signal, while its average output power and PA drain efficiency are 14.1 dBm and 24.1%, respectively. In addition, its ACLR/EVM are -31.5 dBc/ -24.6 dB for a 4.8-Gb/s signal with 11.36-dBm average output power and 17.6% drain efficiency. The spectral purity of the 4.8-Gb/s 64-QAM signal is shown in Fig. 20(c).

A 64-QAM OFDM signal is utilized to verify the performance of the proposed TX for 5G mm-wave systems. Fig. 21 shows the measured constellation for a “400-MHz single-carrier 64-QAM OFDM” signal. With 8.4-dBm output power and 10.8% drain efficiency, TX achieves an EVM of -25.6 dB and an ACLR of -33.5 dBc. The measured EVM of various modulation bandwidths of 50, 100, 200, and 400 MHz versus average output power is reported in Fig. 21(b). Their EVM significantly degrades by increasing their modulation bandwidth at lower average power. The primary limitations

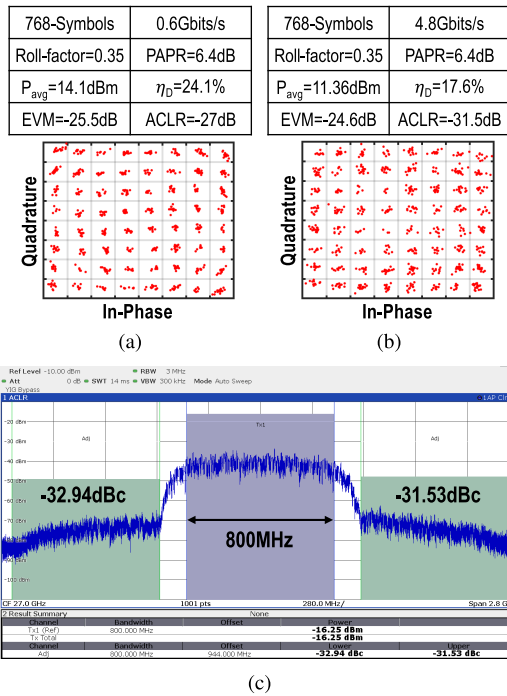


Fig. 20. Measured constellations of a single-carrier 64-QAM signal with (a) 100- and (b) 800-MHz bandwidths. (c) Spectral purity of an 800-MHz 64-QAM signal with 6.4-dB PAPR at 27-GHz carrier frequency.

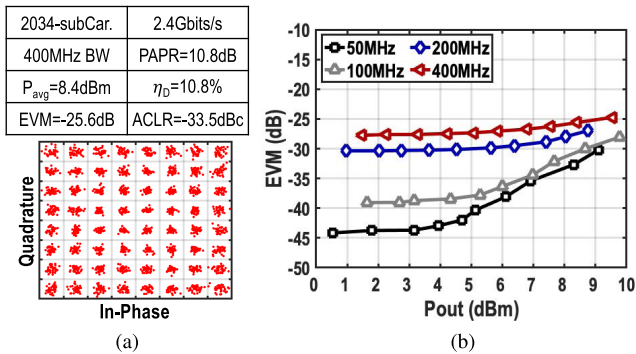


Fig. 21. (a) Measured constellations of a 400-MHz single-carrier 64-QAM OFDM signal at 27 GHz. (b) Measured EVMs versus average power for 50-, 100-, 200-, and 400-MHz 64-QAM OFDM signals.

for high data rate signals are: 1) the gain flatness of the baseband amplifiers; 2) the loss flatness of inter-stage and output matching networks; and 3) the loss flatness of the probe, cables, coupler, and signal analyzer. Likewise, considering all the EVM limitations, e.g., flatness, phase noise, third-order distortion, and thermal noise, measuring -44 dB of EVM for 50-MHz signal confirms that the contribution of IRR and LOFT on EVM is at least less than -44 dB.

To further evaluate the TX performance under different 5G system scenarios, “64-QAM OFDM” signals with 50-, 100-, and 200-MHz component carriers (CCs) and the overall aggregated bandwidth of 800 MHz and 10% guard bands are exploited. Fig. 22(a) shows the spectrum and EVM of an “eight-CC 64-QAM OFDM” signal with 8.4-dBm average power and -27.1 -dB average EVM. The measured average

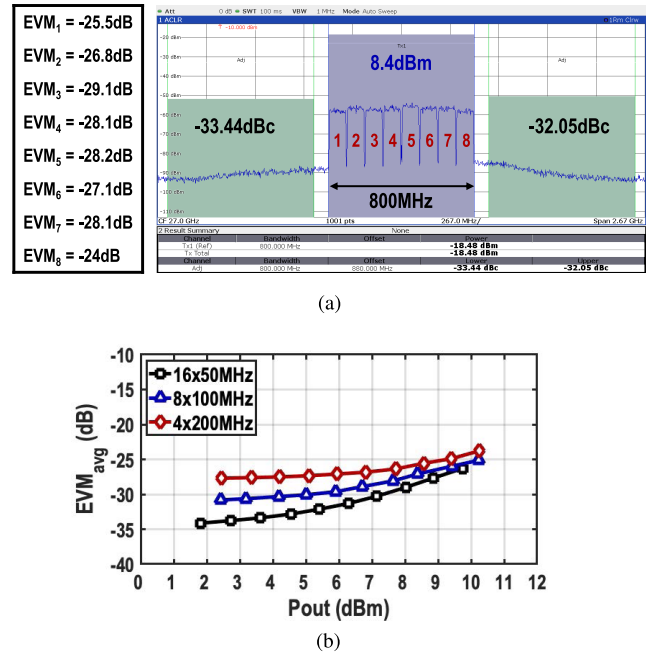


Fig. 22. (a) Spectrum of an eight-CC 64-QAM OFDM signal and measured EVMs of each channel. (b) Measured average EVMs versus average power for four-, eight-, and 16-CC 64-QAM OFDM signals with 800-MHz bandwidth.

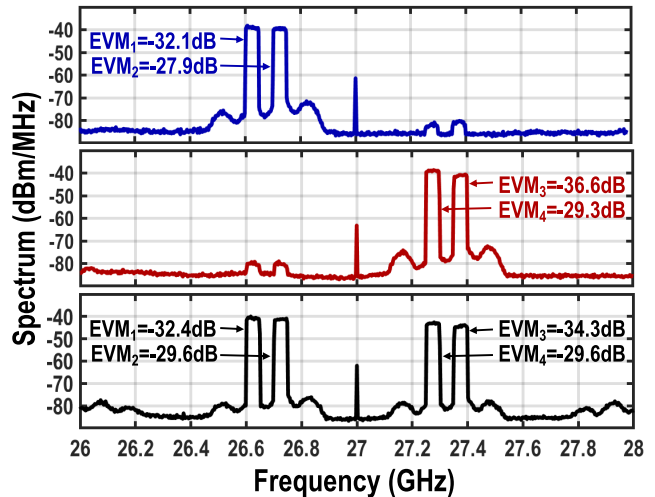


Fig. 23. Measured spectrum and EVMs of a two-CC 50-MHz 64-QAM OFDM signal at lower sideband (blue), a two-CC 50-MHz 64-QAM OFDM signal at upper sideband (red), and a four-CC OFDM signal.

EVM versus output power of four-, eight-, and 16-CC OFDM signals with an 800-MHz aggregated bandwidth are reported in Fig. 22(b). It shows that, for a dedicated data rate, increasing the number of carriers improves its EVM.

Finally, the following measurement sequences are performed to verify the impact of TX’s IRR in a noncontiguous carrier aggregation scenario. First, a two-CC “50-MHz 64-QAM OFDM” signal is applied, whose spectrum (blue) is depicted in Fig. 23. Next, its mirror spectrum (red) is exploited. As illustrated in Fig. 23, the I/Q images of the first case are precisely on top of the second scenario and vice versa. It clearly indicates that a poor IRR performance dramatically

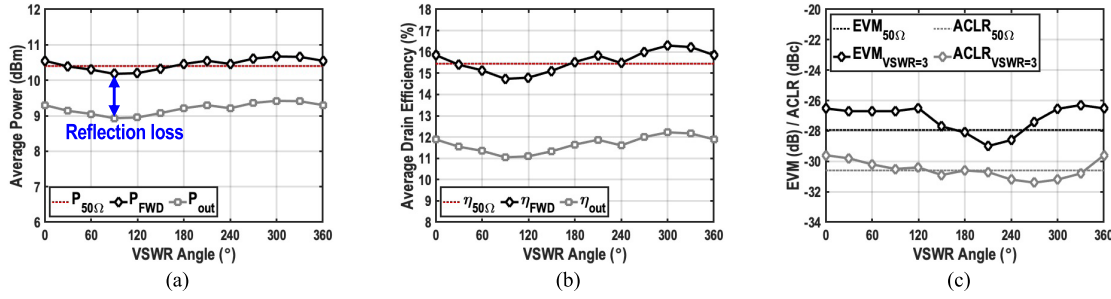


Fig. 24. Measured (a) forward and output average power, (b) average drain efficiency of the related forward and output power, and (c) EVM/ACLR of a 100-MHz 64-QAM signal versus VSWR angle under VSWR = 3 compared to the impedance matched load measurement results.

degrades the EVM. Eventually, the two signals presided at four different locations, i.e., two pairs of mirrored channels, are simultaneously applied. Their measured EVMs are reported, exhibiting that the channels' EVM is not significantly degraded due to the decent I/Q image performance of the proposed double-quadrature TX.

D. VSWR Measurement Results

As discussed in Section III, the robustness of EVM and forward power (P_{FWD}) under load mismatch is crucial in a phased-array system with mutual coupling. The VSWR resilience of the proposed efficiency enhanced BPA is evaluated by measuring a “100-MHz 64-QAM” signal under VSWR of 3. The characterization of the Maury tuner and its calibration is done as described in [34]. Moreover, the bandwidth of the modulated signal is limited by the performance of the load tuner.

To begin with, the TX performance is measured for the matched impedance loading condition. The average output power and drain efficiency are 10.35 dBm and 15%, respectively. In addition, $\text{EVM} = -28$ dB and $\text{ACLR} = -30.6$ dBc are measured (see Fig. 24). Then, for the same input signal level, the tuner is adjusted to provide VSWR = 3 loading condition, and the TX performance is measured for various VSWR angles. Consequently, assuming constant mismatch losses of passive components between the TX and the power sensor, the output power (P_{out}) fluctuation is also the deviation of forward power, reverse power, and gain. The measured P_{out} , P_{FWD} , average drain efficiency, EVM, and ACLR of the modulated signal versus VSWR angle are presented in Fig. 24.

Two drain efficiencies are exhibited in Fig. 24(b): the first drain efficiency is related to P_{FWD} (η_{FWD}), and the second one is related to P_{out} (η_{out}). In the antenna mismatch scenario, as discussed in Section III-A, a portion of forward power is reflected and subsequently is dissipated in the matching network losses and the isolation port. Therefore, P_{out} is considered as the radiated power, and its drain efficiency is then calculated based on P_{out} . However, in the mutual coupling scenario, since the reflected power is the coupled signal generated by the other TX elements in a phased-array system, assuming matched antenna impedance, the radiated power is equal to P_{FWD} . Therefore, the drain efficiency is eventually calculated based on P_{FWD} rather than P_{out} .

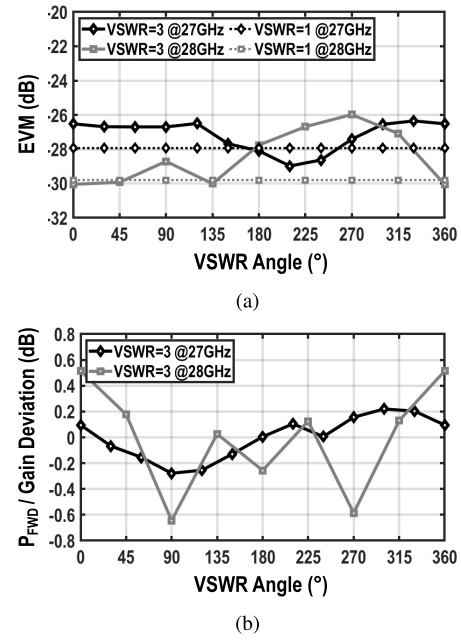


Fig. 25. Measured (a) EVMs and (b) forward power/gain deviations of a 100-MHz 64-QAM signals under VSWR of 1 and 3 at 27 and 28 GHz.

Similar to the average power and its efficiency, the measured EVM and ACLR are relatively robust under VSWR as demonstrated in Fig. 24(c). The maximum EVM and ACLR deviation are 1.65 and 1 dB, respectively. In addition, the measured EVMs under VSWR of 1 and 3 at 27 and 28 GHz are compared in Fig. 25(a). The maximum EVM deviation at 28 GHz is 3.9 dB. The gain and P_{FWD} deviation at 27 and 28 GHz are depicted in Fig. 25(b). At 27 GHz, the maximum deviation is 0.3 dB, which occurs at a 90° VSWR angle. Likewise, at 28 GHz, this deviation is only 0.65 dB.

E. Performance Summary and Comparison

Table I summarizes the measured performance of the proposed double-quadrature TX and compares it to that of prior-art mm-wave TXs/PAs. The TX occupies a 1.38-mm^2 core area slightly larger than [34], which is only a PA. The proposed series-Doherty BPA provides a better output impedance termination than the state of the art while enhancing the

TABLE I
CMOS MM-WAVE TXS/PAS PERFORMANCE COMPARISON

	This Work	mm-Wave 5G Power Amplifiers						mm-Wave TX/Quadrature LO Generators		
		Mannem JSSC 2020	Chappidi TMTT 2020	Wang JSSC 2019	Li JSSC 2020	Huang ISSCC 2021	Shakib ISSCC 2017	Zhao JSSC 2015	Piri JSSC 2018	Kim JSSC 2018
Architecture	Double-quadrature DUC with series-Doherty BPA	Reconfigurable Doherty PA	Broadband Doherty PA	Mixed-signal Doherty PA	Inverse outphasing TX	Continuous Coupler Doherty PA	Analog linear PA	E-band TX	Wideband IQ generator	Transceiver
Technology	40nm CMOS	45nm SOI	65nm CMOS	45nm CMOS	45nm SOI	45nm SOI	40nm CMOS	40nm CMOS	55nm CMOS	28nm CMOS
Supply	1V	2V, 1V	1.1V	2V	2V, 1V	2V, 1V	1.1V	0.9/1.1V	1.2V	1.8/1.05/0.8V
Freq. (GHz)	24 to 30	39	26 to 42	27	29	26 to 60	27	71 to 86	28 to 44	28
Core area (mm ²)	1.38	1.18	1.35*	0.52	0.96	0.62	0.23	0.225	0.195	7.28*
Gain (dB)	21.8 (at 27GHz)	12.4*	13.5*	19.1	30	15.5*	22.4	11	N/A	48
P _{1dB} /P _{sat} (dBm)	20 (at 27GHz)	20.2/20.8	19.2/19.6	22.4/23.3	22.7	21.5/22	13.7/15.1	8.8/12	N/A	9.5
PAE _{peak} /PAE _{avg} (%)	31/26† (at 27GHz)	33.3/22.4	24/20.2	40.1/33.1	41.3/29.6	40.5/32.5	33.7/15.1	N/A	N/A	8.5/5
S ₂₂ (dB)	-22.2 (at 27GHz)	-9*	N/A	-2*	N/A	N/A	-7*	N/A	N/A	-4*
LOFT (dBc)	-45	N/A	N/A	N/A	N/A	N/A	N/A	-40.2†	N/A	-39†
IRR (dB)	>50	N/A	N/A	N/A	N/A	N/A	N/A	40.5†	>40†	62†
TX Efficiency (%)	28.5 (at 27GHz)	N/A	N/A	N/A	N/A	N/A	N/A	15	N/A	N/A
Calibration / DPD	No / No	N/A / No	N/A / No	N/A / No	No / Yes	N/A / No	N/A / No	Yes / No	Yes / N/A	Yes / No
Modulation scheme	64-QAM 8-CC OFDM	64-QAM	64-QAM	64-QAM	64-QAM	64-QAM	64-QAM 8-CC OFDM	64-QAM	N/A	LTE 64-QAM
Data rate (Gb/s)	4.8	800MHz	3	2	6	3	3	800MHz	4.5	20MHz
EVM _{rms} (dB)	-24.6	-27.1	-22.9	-24	-25.3	-25.3	-25	-24	N/A	-33
ACLR (dBc)	-31.45	-32	-25.4	-25	-29.6	-29.8	-28.8	-29	N/A	N/A
P _{avg} (dBm)	11.36	8.4	12.2	9.8	15.9	16	13.4	6.7	N/A	3
PAE _{avg} (%)	17.6 (η _{D,PA})	10.8 (η _{D,PA})	16.1	10.2	29.1	23.8	24.8	11	N/A	3
Modulation / VSWR	64-QAM / 3:1	64-QAM / 3:1	CW / 4:1	N/A	N/A	N/A	N/A	N/A	N/A	N/A
EVM deviation (dB)	1.9/3.9 (at 27/28GHz)	1.6	N/A	N/A	N/A	N/A	N/A	N/A	N/A	N/A
P _{FWD} variation (dB)	0.51/1.2 (at 27/28GHz)	0.62 (2.6)**	2	N/A	N/A	N/A	N/A	N/A	N/A	N/A

* Chip area. *Graphically estimated. †Drain efficiency of the PAs and pre-drivers. ‡After calibration. **P_{1dB} (Gain) variations: gain variation is graphically estimated.

efficiency over a wide operational bandwidth of 24–30 GHz with 40% peak drain efficiency. The measured drain efficiency at P₁ dB and 6-dB PBO are comparable to [27] and [32], which has the best PAE at P₁ dB and 6-dB PBO, respectively. Moreover, under VSWR, the proposed TX achieves less than 0.3- and 1.9-dB forward power and EVM deviation, respectively. Furthermore, the proposed double-quadrature modulator offers wideband IRR without calibration, outperforming state-of-the-art TXs utilizing the I/Q imbalance calibration. In addition, due to the symmetrical layout of the I/Q modulator and mismatch considerations, the uncalibrated LOFT of three measured chips over various operational frequencies is less than -44 dBc.

VI. CONCLUSION

In this article, an efficient broadband TX comprising a DQ-DUC and a series-Doherty BPA in 40-nm bulk CMOS is presented for 5G mm-wave phased-array systems. The proposed EEBPA structure provides 20-dBm output power while achieving 6-dB PBO efficiency enhancement under VSWR caused by the mutual coupling of phased-array systems. Moreover, the proposed double-quadrature direct-upconversion architecture inherently offers high IRR. Its second image-rejection stage is elegantly combined with the proposed quadrature hybrid BPA, resulting in superior I/Q image performance. Due to the symmetric layout and mismatch consideration, the measured uncalibrated LOFT is among the best. Occupying a 1.38-mm² core area, TX delivers more than 20-dBm P₁ dB with 40% drain efficiency while achieving reasonable PBO drain efficiency and linearity. In addition, this prototype obtained excellent uncalibrated IRR and LOFT performance.

APPENDIX A

The mathematical relationship of the image rejection at the second stage of the proposed DQ-DUC is elaborated. In this context, $x_{BB,I}$ and $x_{BB,Q}$ are I/Q baseband signals. Considering this, the I/Q LO signals with phase and amplitude mismatches are represented as follows:

$$LO_I = \left(1 + \frac{\epsilon}{2}\right) \cos\left(\omega_c t + \frac{\Delta\theta}{2}\right) \quad (7)$$

$$LO_Q = \left(1 - \frac{\epsilon}{2}\right) \sin\left(\omega_c t - \frac{\Delta\theta}{2}\right) \quad (8)$$

where ϵ and $\Delta\theta$ are amplitude and phase error of I/Q LO signals. The RF₀ and RF₉₀ signals, as shown in Fig. 3, can be calculated as

$$RF_0 = x_{BB,I} LO_I - x_{BB,Q} LO_Q \quad (9)$$

$$RF_{90} = x_{BB,Q} LO_I + x_{BB,I} LO_Q. \quad (10)$$

Now, by placing (7) and (8) in (9) and (10), the combined RF signal at the PA port of QHC can be calculated as

$$\begin{aligned} RF &= RF_0 + H(RF_{90}) = x_{BB,I} \left(1 + \frac{\epsilon}{2}\right) \cos\left(\omega_c t + \frac{\Delta\theta}{2}\right) \\ &\quad - x_{BB,Q} \left(1 - \frac{\epsilon}{2}\right) \sin\left(\omega_c t - \frac{\Delta\theta}{2}\right) + x_{BB,Q} \left(1 + \frac{\epsilon}{2}\right) \\ &\quad \times \cos\left(\omega_c t + \frac{\Delta\theta}{2} - \frac{\pi}{2}\right) \\ &\quad + x_{BB,I} \left(1 - \frac{\epsilon}{2}\right) \sin\left(\omega_c t - \frac{\Delta\theta}{2} - \frac{\pi}{2}\right) \Rightarrow \\ RF &= x_{BB,I} \left[\left(1 + \frac{\epsilon}{2}\right) \cos\left(\omega_c t + \frac{\Delta\theta}{2}\right) + \left(1 - \frac{\epsilon}{2}\right) \cos\left(\omega_c t - \frac{\Delta\theta}{2}\right)\right] \end{aligned}$$

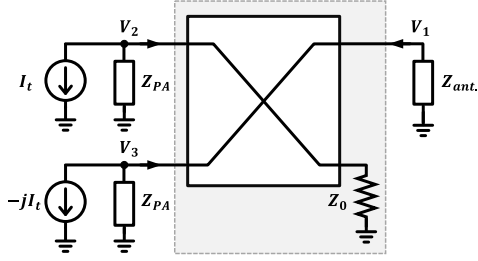


Fig. 26. Z-parameter analysis of a BPA in antenna mismatch scenario assuming identical PAs.

$$-x_{BB,Q} \left[\left(1 - \frac{\epsilon}{2}\right) \sin\left(\omega_c t - \frac{\Delta\theta}{2}\right) + \left(1 + \frac{\epsilon}{2}\right) \sin\left(\omega_c t + \frac{\Delta\theta}{2}\right) \right] \quad (11)$$

where $H(\text{RF}_{90})$ is the Hilbert transform of the RF90 waveform. We can derive a similar expression for the combined signal at the isolation port of QHC. Performing some mathematical expansions and simplifications (11) using well-known trigonometric identities, RF can be expressed as

$$\text{RF} = 2 \cos\left(\frac{\Delta\theta}{2}\right) (x_{BB,I} \cos(\omega_c t) - x_{BB,Q} \sin(\omega_c t)) - \epsilon \sin\left(\frac{\Delta\theta}{2}\right) (x_{BB,Q} \cos(\omega_c t) + x_{BB,I} \sin(\omega_c t)). \quad (12)$$

This expression proves that the amplitude and phase mismatches are canceled, and thus, the desired output modulated signal does not contain any I/Q image component.

APPENDIX B

Fig. 26 shows a schematic for an impedance analysis. In this context, two test current sources are applied simultaneously to both PA ports to obtain the related Z-impedance matrix. To simplify the calculations, we assume that an ideal Z_0 resistor terminates the isolation port. Consequently, the combiner can be considered as a three ports network, and therefore, the S-parameter and Z-parameter matrixes are squeezed to [64]

$$S = \begin{bmatrix} 0 & j & 1 \\ j & 0 & 0 \\ 1 & 0 & 0 \end{bmatrix} \quad (13)$$

$$Z = Z_0 \begin{bmatrix} 1 & -j\sqrt{2} & \sqrt{2} \\ -j\sqrt{2} & 0 & -j \\ \sqrt{2} & -j & 2 \end{bmatrix}. \quad (14)$$

Applying KCL analysis at the three ports, the impedance equations can be calculated by solving the following equation:

$$\begin{bmatrix} V_1 \\ V_2 \\ V_3 \end{bmatrix} = Z_0 \begin{bmatrix} 1 & -j\sqrt{2} & \sqrt{2} \\ -j\sqrt{2} & 0 & -j \\ \sqrt{2} & -j & 2 \end{bmatrix} \begin{bmatrix} -\frac{V_1}{Z_{\text{ant}}} \\ -I_t - \frac{V_2}{Z_{\text{PA}}} \\ jI_t - \frac{V_3}{Z_{\text{PA}}} \end{bmatrix}. \quad (15)$$

Hence, the impedance driven by two PAs are calculated as

$$Z_{L1} = \frac{V_2}{I_t + \frac{V_2}{Z_{\text{PA}}}} = Z_0 \frac{Z_0^2 + (Z_{\text{ant}} - Z_{\text{PA}})Z_0 + 3Z_{\text{PA}}Z_{\text{ant}}}{3Z_0^2 + (Z_{\text{PA}} - Z_{\text{ant}})Z_0 + Z_{\text{PA}}Z_{\text{ant}}}. \quad (16)$$

$$Z_{L2} = \frac{V_3}{-jI_t + \frac{V_3}{Z_{\text{PA}}}} = Z_0 \frac{Z_0^2 + (Z_{\text{ant}} + 3Z_{\text{PA}})Z_0 - Z_{\text{PA}}Z_{\text{ant}}}{-Z_0^2 + (Z_{\text{PA}} + 3Z_{\text{ant}})Z_0 + Z_{\text{PA}}Z_{\text{ant}}}. \quad (17)$$

ACKNOWLEDGMENT

imec-Leuven is acknowledged for handling the tape-out. The authors would like to thank Atef Akhnoukh and Zu-Yao Chang for their strong support during the design, fabrication, and measurement. They also thank Hitech BV and Maury-MW for providing measurement support and Milad Kalantari for helpful discussions.

REFERENCES

- [1] E. G. Larsson, O. Edfors, F. Tufvesson, and T. L. Marzetta, "Massive MIMO for next generation wireless systems," *IEEE Commun. Mag.*, vol. 52, no. 2, pp. 186–195, Feb. 2014.
- [2] M. Shafi *et al.*, "5G: A tutorial overview of standards, trials, challenges, deployment, and practice," *IEEE J. Sel. Areas Commun.*, vol. 35, no. 6, pp. 1201–1221, Jun. 2017.
- [3] I. Ahmed *et al.*, "A survey on hybrid beamforming techniques in 5G: Architecture and system model perspectives," *IEEE Commun. Surveys Tuts.*, vol. 20, no. 4, pp. 3060–3097, 4th Quart., 2018.
- [4] S. A. Busari, K. M. S. Huq, S. Mumtaz, L. Dai, and J. Rodriguez, "Millimeter-wave massive MIMO communication for future wireless systems: A survey," *IEEE Commun. Surveys Tuts.*, vol. 20, no. 2, pp. 836–869, 2nd Quart., 2018.
- [5] T. Tuovinen, N. Tervo, and A. Pärssinen, "Analyzing 5G RF system performance and relation to link budget for directive MIMO," *IEEE Trans. Antennas Propag.*, vol. 65, no. 12, pp. 6636–6645, Dec. 2017.
- [6] B. Yang, Z. Yu, J. Lan, R. Zhang, J. Zhou, and W. Hong, "Digital beamforming-based massive MIMO transceiver for 5G millimeter-wave communications," *IEEE Trans. Microw. Theory Techn.*, vol. 66, no. 7, pp. 3403–3418, Jul. 2018.
- [7] A. K. Gupta and J. F. Buckwalter, "Linearity considerations for low-EVM, millimeter-wave direct-conversion modulators," *IEEE Trans. Microw. Theory Techn.*, vol. 60, no. 10, pp. 3272–3285, Oct. 2012.
- [8] D. Zhao and P. Reynaert, "A 40 nm CMOS E-band transmitter with compact and symmetrical layout floor-plans," *IEEE J. Solid-State Circuits*, vol. 50, no. 11, pp. 2560–2571, Nov. 2015.
- [9] P. Y. Wu, A. K. Gupta, and J. F. Buckwalter, "A dual-band millimeter-wave direct-conversion transmitter with quadrature error correction," *IEEE Trans. Microw. Theory Techn.*, vol. 62, no. 12, pp. 3118–3130, Dec. 2014.
- [10] R. Wu *et al.*, "64-QAM 60-GHz CMOS transceivers for IEEE 802.11ad/ay," *IEEE J. Solid-State Circuits*, vol. 52, no. 11, pp. 2871–2891, Nov. 2017.
- [11] H.-T. Kim *et al.*, "A 28-GHz CMOS direct conversion transceiver with packaged 2×4 antenna array for 5G cellular system," *IEEE J. Solid-State Circuits*, vol. 53, no. 5, pp. 1245–1259, May 2018.
- [12] F. Piri, M. Bassi, N. R. Lacaita, A. Mazzanti, and F. Svelto, "A PVT-tolerant >40-dB IRR, 44% fractional-bandwidth ultra-wideband mm-wave quadrature LO generator for 5G networks in 55-nm CMOS," *IEEE J. Solid-State Circuits*, vol. 53, no. 12, pp. 3576–3586, Dec. 2018.
- [13] J. Pang *et al.*, "A 50.1-Gb/s 60-GHz CMOS transceiver for IEEE 802.11ay with calibration of LO feedthrough and I/Q imbalance," *IEEE J. Solid-State Circuits*, vol. 54, no. 5, pp. 1375–1390, May 2019.
- [14] F. Piri, E. Rahimi, M. Bassi, F. Svelto, and A. Mazzanti, "70–90-GHz self-tuned polyphase filter for wideband I/Q LO generation in a 55-nm BiCMOS transmitter," *IEEE Solid-State Circuits Lett.*, vol. 2, no. 9, pp. 155–158, Sep. 2019.

- [15] A. Rezola *et al.*, "Temperature-dependent I/Q imbalance compensation in ultra-wideband millimeter-wave multi-gigabit transmitters," *IEEE Trans. Microw. Theory Techn.*, vol. 68, no. 1, pp. 340–352, Jan. 2020.
- [16] B. Sadhu *et al.*, "A 28-GHz 32-element TRX phased-array IC with concurrent dual-polarized operation and orthogonal phase and gain control for 5G communications," *IEEE J. Solid-State Circuits*, vol. 52, no. 12, pp. 3373–3391, Dec. 2017.
- [17] H. Hashemi, "Millimeter-wave power amplifiers & transmitters," in *Proc. IEEE Custom Integr. Circuits Conf. (CICC)*, Apr. 2017, pp. 1–8.
- [18] D. Zhao and P. Reynaert, "A 40-nm CMOS E-band 4-way power amplifier with neutralized bootstrapped cascode amplifier and optimum passive circuits," *IEEE Trans. Microw. Theory Techn.*, vol. 63, no. 12, pp. 4083–4089, Dec. 2015.
- [19] S. Shakib, M. Elkholy, J. Dunworth, V. Aparin, and K. Entesari, "2.7 A wideband 28GHz power amplifier supporting 8×100MHz carrier aggregation for 5G in 40nm CMOS," in *IEEE Int. Solid-State Circuits Conf. (ISSCC) Dig. Tech. Papers*, Feb. 2017, pp. 44–45.
- [20] N. Rostomyan, M. Özen, and P. Asbeck, "28 GHz Doherty power amplifier in CMOS SOI with 28% back-Off PAE," *IEEE Microw. Compon. Lett.*, vol. 28, no. 5, pp. 446–448, May 2018.
- [21] D. Zhao and P. Reynaert, "An E-band power amplifier with broadband parallel-series power combiner in 40-nm CMOS," *IEEE Trans. Microw. Theory Techn.*, vol. 63, no. 2, pp. 683–690, Feb. 2015.
- [22] W.-C. Huang, J.-L. Lin, Y.-H. Lin, and H. Wang, "A K-band power amplifier with 26-dBm output power and 34% PAE with novel inductance-based neutralization in 90-nm CMOS," in *Proc. IEEE Radio Freq. Integr. Circuits Symp. (RFIC)*, Jun. 2018, pp. 228–231.
- [23] C.-W. Wu, Y.-H. Lin, Y.-H. Hsiao, C.-F. Chou, Y.-C. Wu, and H. Wang, "Design of a 60-GHz high-output power stacked-FET power amplifier using transformer-based voltage-type power combining in 65-nm CMOS," *IEEE Trans. Microw. Theory Techn.*, vol. 66, no. 10, pp. 4595–4607, Oct. 2018.
- [24] D. Manente, F. Padovan, D. Seebacher, M. Bassi, and A. Bevilacqua, "A 28-GHz stacked power amplifier with 20.7-dBm output P_{1dB} in 28-nm bulk CMOS," *IEEE Solid-State Circuits Lett.*, vol. 3, pp. 170–173, 2020.
- [25] S. Li, T. Chi, J.-S. Park, H. T. Nguyen, and H. Wang, "A 28-GHz flip-chip packaged Chireix transmitter with on-antenna outphasing active load modulation," *IEEE J. Solid-State Circuits*, vol. 54, no. 5, pp. 1243–1253, May 2019.
- [26] D. Zhao, S. Kulkarni, and P. Reynaert, "A 60-GHz outphasing transmitter in 40-nm CMOS," *IEEE J. Solid-State Circuits*, vol. 47, no. 12, pp. 3172–3183, Dec. 2012.
- [27] S. Li, M.-Y. Huang, D. Jung, T.-Y. Huang, and H. Wang, "A MM-wave current-mode inverse outphasing transmitter front-end: A circuit duality of conventional voltage-mode outphasing," *IEEE J. Solid-State Circuits*, vol. 56, no. 6, pp. 1732–1744, Jun. 2021.
- [28] E. Kaymaksut, D. Zhao, and P. Reynaert, "Transformer-based Doherty power amplifiers for mm-wave applications in 40-nm CMOS," *IEEE Trans. Microw. Theory Techn.*, vol. 63, no. 4, pp. 1186–1192, Apr. 2015.
- [29] C. R. Chappidi, X. Wu, and K. Sengupta, "Simultaneously broadband and back-off efficient mm-wave PAs: A multi-port network synthesis approach," *IEEE J. Solid-State Circuits*, vol. 53, no. 9, pp. 2543–2559, Jun. 2018.
- [30] H. T. Nguyen, T. Chi, S. Li, and H. Wang, "A linear high-efficiency millimeter-wave CMOS Doherty radiator leveraging multi-feed on-antenna active load modulation," *IEEE J. Solid-State Circuits*, vol. 53, no. 12, pp. 3587–3598, Dec. 2018.
- [31] H. T. Nguyen, S. Li, and H. Wang, "4.6 A mm-wave 3-way linear Doherty radiator with multi antenna coupling and on-antenna current-scaling series combiner for deep power back-off efficiency enhancement," in *IEEE Int. Solid-State Circuits Conf. (ISSCC) Dig. Tech. Papers*, Feb. 2019, pp. 84–86.
- [32] F. Wang, T.-W. Li, S. Hu, and H. Wang, "A super-resolution mixed-signal Doherty power amplifier for simultaneous linearity and efficiency enhancement," *IEEE J. Solid-State Circuits*, vol. 54, no. 12, pp. 3421–3436, Dec. 2019.
- [33] S. Hu, F. Wang, and H. Wang, "A 28-/37-/39-GHz linear Doherty power amplifier in silicon for 5G applications," *IEEE J. Solid-State Circuits*, vol. 54, no. 6, pp. 1586–1599, Jun. 2019.
- [34] N. S. Mannem, M.-Y. Huang, T.-Y. Huang, and H. Wang, "A reconfigurable hybrid series/parallel Doherty power amplifier with antenna VSWR resilient performance for MIMO arrays," *IEEE J. Solid-State Circuits*, vol. 55, no. 12, pp. 3335–3348, Dec. 2020.
- [35] F. Wang and H. Wang, "24.1 A 24-to-30GHz watt-level broadband linear Doherty power amplifier with multi-primary distributed-active-transformer power-combining supporting 5G NR FR2 64-QAM with >19dBm average pout and >19% average PAE," in *IEEE Int. Solid-State Circuits Conf. (ISSCC) Dig. Tech. Papers*, Feb. 2020, pp. 362–364.
- [36] H. T. Nguyen and H. Wang, "A coupler-based differential mm-wave Doherty power amplifier with impedance inverting and scaling baluns," *IEEE J. Solid-State Circuits*, vol. 55, no. 5, pp. 1212–1223, May 2020.
- [37] Z. Zong *et al.*, "A 28-GHz SOI-CMOS Doherty power amplifier with a compact transformer-based output combiner," *IEEE Trans. Microw. Theory Techn.*, vol. 69, no. 6, pp. 2795–2808, Jun. 2021.
- [38] T.-Y. Huang, N. S. Mannem, S. Li, D. Jung, M.-Y. Huang, and H. Wang, "26.1 A 26-to-60GHz continuous coupler-Doherty linear power amplifier for over-an-octave back-off efficiency enhancement," in *IEEE Int. Solid-State Circuits Conf. (ISSCC) Dig. Tech. Papers*, Feb. 2021, pp. 354–356.
- [39] F. M. Barradas, P. M. Tomé, J. M. Gomes, T. R. Cunha, P. M. Cabral, and J. C. Pedro, "Power, linearity, and efficiency prediction for MIMO arrays with antenna coupling," *IEEE Trans. Microw. Theory Techn.*, vol. 65, no. 12, pp. 5284–5297, Dec. 2017.
- [40] S. K. Dhar, A. Abdelhafiz, M. Aziz, M. Helaoui, and F. M. Ghannouchi, "A reflection-aware unified modeling and linearization approach for power amplifier under mismatch and mutual coupling," *IEEE Trans. Microw. Theory Techn.*, vol. 66, no. 9, pp. 4147–4157, Sep. 2018.
- [41] X. Chen, S. Zhang, and Q. Li, "A review of mutual coupling in MIMO systems," *IEEE Access*, vol. 6, pp. 24706–24719, 2018.
- [42] C. Fager, T. Eriksson, F. Barradas, K. Hausmair, T. Cunha, and J. C. Pedro, "Linearity and efficiency in 5G transmitters: New techniques for analyzing efficiency, linearity, and linearization in a 5G active antenna transmitter context," *IEEE Microw. Mag.*, vol. 20, no. 5, pp. 35–49, May 2019.
- [43] X. Chen, M. Abdullah, Q. Li, J. Li, A. Zhang, and T. Svensson, "Characterizations of mutual coupling effects on switch-based phased array antennas for 5G millimeter-wave mobile communications," *IEEE Access*, vol. 7, pp. 31376–31384, 2019.
- [44] S. M. Bowers, K. Sengupta, K. Dasgupta, B. D. Parker, and A. Hajimiri, "Integrated self-healing for mm-wave power amplifiers," *IEEE Trans. Microw. Theory Techn.*, vol. 61, no. 3, pp. 1301–1315, Mar. 2013.
- [45] C. R. Chappidi, T. Sharma, and K. Sengupta, "Multi-port active load pulling for mm-wave 5G power amplifiers: Bandwidth, back-off efficiency, and VSWR tolerance," *IEEE Trans. Microw. Theory Techn.*, vol. 68, no. 7, pp. 2998–3016, Jul. 2020.
- [46] T. Dinc, A. Nagulu, and H. Krishnaswamy, "A millimeter-wave non-magnetic passive SOI CMOS circulator based on spatio-temporal conductivity modulation," *IEEE J. Solid-State Circuits*, vol. 52, no. 12, pp. 3276–3292, Dec. 2017.
- [47] A. Nagulu and H. Krishnaswamy, "28.5 non-magnetic 60GHz SOI CMOS circulator based on loss/dispersion-engineered switched bandpass filters," in *IEEE Int. Solid-State Circuits Conf. (ISSCC) Dig. Tech. Papers*, Feb. 2019, pp. 446–448.
- [48] R. Garg, S. Jain, P. Dania, and A. Natarajan, "14.3 A 26GHz full-duplex circulator receiver with 53dB/400MHz(40dB/800MHz) self-interference cancellation for mm-wave repeaters," in *IEEE Int. Solid-State Circuits Conf. (ISSCC) Dig. Tech. Papers*, Feb. 2021, pp. 222–224.
- [49] F. Torres, M. De Matos, A. Cathelin, and E. Kerherve, "A 31 GHz 2-stage reconfigurable balanced power amplifier with 32.6dB power gain, 25.5% PAE_{max} and 17.9dBm p_{sat} in 28nm FD-SOI CMOS," in *Proc. IEEE Radio Freq. Integr. Circuits Symp. (RFIC)*, Jun. 2018, pp. 236–239.
- [50] S. Shahramian, M. J. Holyoak, A. Singh, and Y. Baeyens, "A fully integrated 384-element, 16-tile, W-band phased array with self-alignment and self-test," *IEEE J. Solid-State Circuits*, vol. 54, no. 9, pp. 2419–2434, Sep. 2019.
- [51] M. Pashaeifar, L. C. N. de Vreede, and M. S. Alavi, "14.4 A 24-to-30GHz double-quadrature direct-upconversion transmitter with mutual-coupling-resilient series-Doherty balanced PA for 5G MIMO arrays," in *IEEE Int. Solid-State Circuits Conf. (ISSCC) Dig. Tech. Papers*, Feb. 2021, pp. 223–225.
- [52] S. Kulkarni, D. Zhao, and P. Reynaert, "Design of an optimal layout polyphase filter for millimeter-wave quadrature LO generation," *IEEE Trans. Circuits Syst. II, Exp. Briefs*, vol. 60, no. 4, pp. 202–206, Apr. 2013.
- [53] J. S. Park and H. Wang, "A transformer-based poly-phase network for ultra-broadband quadrature signal generation," *IEEE Trans. Microw. Theory Techn.*, vol. 63, no. 12, pp. 4444–4457, Dec. 2015.

- [54] M.-Y. Huang, T. Chi, S. Li, T.-Y. Huang, and H. Wang, "A 24.5–43.5-GHz ultra-compact CMOS receiver front end with calibration-free instantaneous full-band image rejection for multiband 5G massive MIMO," *IEEE J. Solid-State Circuits*, vol. 55, no. 5, pp. 1177–1186, May 2020.
- [55] J. Crols and M. S. J. Steyaert, "A single-chip 900 MHz CMOS receiver front-end with a high performance low-IF topology," *IEEE J. Solid-State Circuits*, vol. 30, no. 12, pp. 1483–1492, Dec. 1995.
- [56] J. C. Rudell *et al.*, "A 1.9-GHz wide-band IF double conversion CMOS receiver for cordless telephone applications," *IEEE J. Solid-State Circuits*, vol. 32, no. 12, pp. 2071–2088, Dec. 1997.
- [57] B. Razavi, "RF microelectronics," in *Communications Engineering & Emerging Technology Series From Ted Rappaport*. London, U.K.: Pearson, 2011.
- [58] H. Jeon *et al.*, "A triple-mode balanced linear CMOS power amplifier using a switched-quadrature coupler," *IEEE J. Solid-State Circuits*, vol. 47, no. 9, pp. 2019–2032, Sep. 2012.
- [59] G. Nikandish, R. B. Staszewski, and A. Zhu, "Breaking the bandwidth limit: A review of broadband Doherty power amplifier design for 5G," *IEEE Microw. Mag.*, vol. 21, no. 4, pp. 57–75, Apr. 2020.
- [60] H. Gao *et al.*, "A 48–61 GHz LNA in 40-nm CMOS with 3.6 dB minimum NF employing a metal slotting method," in *Proc. IEEE Radio Freq. Integr. Circuits Symp. (RFIC)*, May 2016, pp. 154–157.
- [61] D. Zhao and P. Reynaert, "A 60-GHz dual-mode class AB power amplifier in 40-nm CMOS," *IEEE J. Solid-State Circuits*, vol. 48, no. 10, pp. 2323–2337, Oct. 2013.
- [62] M. Vigilante and P. Reynaert, "A wideband class-AB power amplifier with 29–57-GHz AM–PM compensation in 0.9-V 28-nm bulk CMOS," *IEEE J. Solid-State Circuits*, vol. 53, no. 5, pp. 1288–1301, May 2018.
- [63] S. Kshattray, W. Choi, C. Yu, and K. O. Kenneth, "Compact diode connected MOSFET detector for on-chip millimeter-wave voltage measurements," *IEEE Microw. Wireless Compon. Lett.*, vol. 26, no. 5, pp. 349–351, May 2016.
- [64] G. Gonzalez, *Microwave Transistor Amplifiers: Analysis and Design*. Upper Saddle River, NJ, USA: Prentice-Hall, 1997.



Masoud Pashaeifar (Student Member, IEEE) received the B.Sc. degree from the Shahid Bahonar University of Kerman, Kerman, Iran, in 2011, and the M.Sc. degree in electrical engineering, circuits, and systems from the University of Tehran, Tehran, Iran, in 2013. He is currently pursuing the Ph.D. degree with the Delft University of Technology, Delft, The Netherlands.

He was the Head of the Hardware Research Group, Bakhtar Communication Company, Tehran. His current research interests include mm-wave transceivers

for 5G cellular applications.

Mr. Pashaeifar has been serving as a Reviewer for the IEEE TRANSACTIONS ON CIRCUITS AND SYSTEMS (TCAS-I) since 2020.



Leo C. N. de Vreede (Senior Member, IEEE) received the Ph.D. degree (*cum laude*) from the Delft University of Technology, Delft, The Netherlands, in 1996.

In 1996, he was appointed as an Assistant Professor at the Delft University of Technology, working on the nonlinear distortion behavior of active devices. In 1999 and 2015, he was appointed, respectively, as an Associate Professor and a Full Professor at the Delft University of Technology, where he became responsible for the Electronic Research Laboratory (ERL/ELCA). During that period, he worked on solutions for improved linearity and RF performance at the device, circuit, and system levels. He is a Co-Founder/Advisor of Anteverta-mw, Eindhoven, The Netherlands, a company that is specialized in RF device characterization. He has (co)authored more than 120 IEEE refereed conference papers and journal articles. He holds several patents. His current interests include RF measurement systems, RF technology optimization, and (digital-intensive) energy-efficient/wideband circuit/system concepts for wireless applications.

Dr. de Vreede was a (co)recipient of the IEEE Microwave Prize in 2008 and a Mentor of the Else Kooi Prize Awarded Ph.D. Work in 2010 and the Dow Energy Dissertation Prize Awarded Ph.D. Work in 2011. He was a recipient of the TUD Entrepreneurial Scientist Award in 2015. He (co)guided several students that won (best) paper awards at the Bipolar/BiCMOS Circuits and Technology Meeting (BCTM), the Program for Research on Integrated Systems and Circuits (PRORISC), the European Solid-state Circuits and Devices Conference (ESSDERC), the International Microwave Symposium (IMS), the Radio-Frequency Integration Technology (RFIT), and the Radio Frequency Integrated Circuits Symposium (RFIC).



Morteza S. Alavi (Member, IEEE) received the B.Sc. degree in electrical engineering from Iran University of Science and Technology, Tehran, Iran, in 2003, the M.Sc. degree in electrical engineering from the University of Tehran, Tehran, in 2006, and the Ph.D. degree in electrical engineering from the Delft University of Technology (TU-Delft), Delft, The Netherlands, in 2014.

He was a Co-Founder and the CEO of DitiQ B.V., The Netherlands, a local company developing energy-efficient, wideband wireless transmitters

for the next generation of the cellular network. Since September 2016, he joined the ELCA Research Group, TU-Delft, where he is currently a tenured Assistant Professor. He has coauthored *Radio-Frequency Digital-to-Analog Converter* (Elsevier, 2016). His main research interest is designing high-frequency and high-speed wireless/cellular communication and sensor systems, as well as in the field of wireline transceivers.

Dr. Alavi was the Best Paper Award recipient of the 2011 IEEE International Symposium on Radio-Frequency Integrated Technology (RFIT). He was a recipient of the Best Student Paper Award (Second Place) of the 2013 Radio-Frequency Integrated Circuits (RFIC) Symposium. His Ph.D. student also won the Best Student Paper Award (First Place) of the 2017 RFIC Symposium held in Honolulu, HI, USA. He also serves as a Reviewer for the IEEE JOURNAL OF SOLID-STATE CIRCUITS (JSSC), the IEEE TRANSACTIONS ON MICROWAVE THEORY AND TECHNIQUES (TMTT), IEEE TRANSACTIONS ON CIRCUITS AND SYSTEMS (TCAS-I), IEEE TRANSACTIONS ON VERY LARGE SCALE INTEGRATION (VLSI) SYSTEMS (T-VLSI), and *ICEIE Transactions on Communications*.